CERN-ACC-NOTE-2022-0014

CERN-PBC-Notes-2022-006

22 April 2022
rebecca.louise.ramjiawan@cern.ch

SPS MD5044 : machine stability characterisation of Gamma Factory SPS Proof-of-Principle Experiment

R. Ramjiawan, H. Bartosik, Y. Dutheil, W. Hofle, M. W. Krasny, A. Martens, Y. Papaphilippou, A. Petrenko, F. M. Velotti
CERN, CH-1211 Geneva, Switzerland

Keywords: Gamma Factory, GF-SPS-PoP, SPS, beam stability, beam trajectory, radial steering, beam position monitor

Summary

The Gamma Factory (GF) initiative proposes an innovative method of producing high-energy, high-intensity photon beams via the laser-excitation and subsequent decay of relativistic partially stripped ions stored in the CERN LHC. An initial proof-of-principle experiment in the CERN SPS (GF-SPS-PoP) was proposed in 2019 [3] and would demonstrate the key concepts of this method. Such an experiment would require good control and stability of the SPS beam position and momentum, this was investigated during Machine Development (MD) study 5044. The SPS beam stability at the proposed GF interaction point (IP) location was measured over the millisecond-to-second time-scale. To demonstrate control over the position and angle of the beam at the IP, four-corrector orbit bumps were implemented. The use of radial steering for varying the revolution frequency and, thus, the orbit radius was tested. Here we present the results from these studies towards demonstrating that the stability and control achievable in the CERN SPS would be suitable for the GF Proof-of-Principle experiment.

Contents

1 Introduction

The aims of this study are to investigate the SPS beam stability and to demonstrate control over the beam position at the proposed GF IP (Fig. 1). For the GF-SPS-PoP experiment, the considered transverse ion beam sizes at the IP are $\sigma_x = 1.047\,\text{mm}$ and $\sigma_y = 0.83\,\text{mm}$ [3]. The beam jitter at the IP should be kept much less than these values.

For this MD, the SPS was configured with a fixed frequency on the flat-top and a knob (radial steering) to change this frequency. The flat-top energy was 236.1 GeV with a length of 10 s. A cycled beam was used with single-bunch injection with $1 \times 10^{10} p^+$ per bunch. Q20 optics were used.

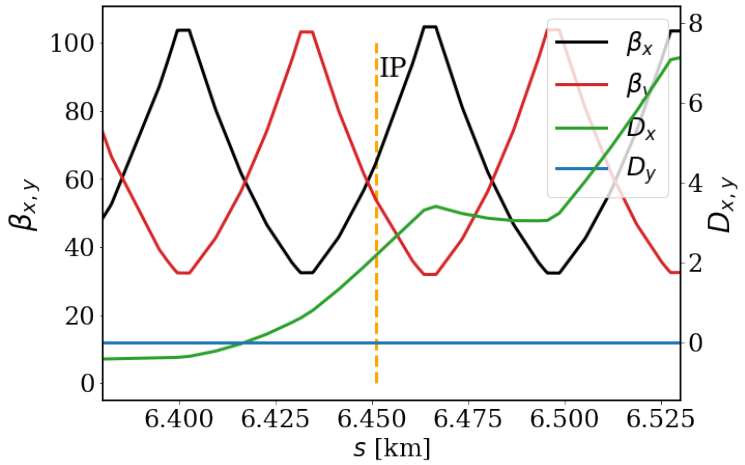

Figure 1: MAD-X simulation of a section of the SPS showing Twiss parameters β_x (black), β_y (red) and dispersion D_x (green) and D_y (blue); the location of the proposed GF IP is indicated.

To determine the beam stability at the GF IP, measurements were taken at several surrounding BPMs and the beamline model was used to interpolate these measurements to the IP. Two BPM configurations were used to span the timescales of interest to the GF-SPS-PoP experiment. For timescales less than 184 ms, 'Capture Acquisition' mode allowed for turn-by-turn data from up to 8000 turns to be acquired. In this mode, it was possible to perform only one capture per cycle. For timescales longer than 184 ms, 'Orbit' mode was used, with 1 ms averaging of the beam position and 1 kHz sampling.

Correctors were used to vary the beam position and angle at the IP. The maximum corrector current was ±3.5 A allowing for beam deflections of ∼40 μrad and ∼21 μrad horizontally and vertically, respectively.

2 Beam position stability at the GF IP

The measured beam position jitter is presented in Fig. 2 for the two BPM modes. From these data, the horizontal and vertical r.m.s position variations were approximately $\sigma_x = 450\,\mu\text{m}$ and $\sigma_y = 250\,\mu\text{m}$, for the turn-by-turn data.

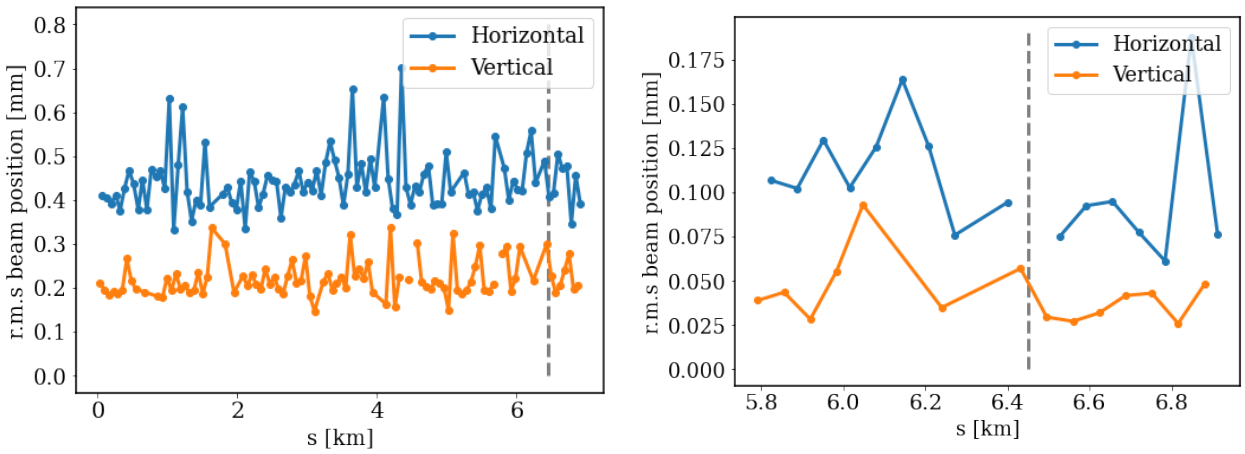

(a) (b)

Figure 2: Measured r.m.s of the beam position for (a) acquisition mode, turn-by-turn BPM data (2000 turns) for BPMs around the SPS and (b) orbit mode BPM data averaged over 1 ms (7000 samples) for the region surrounding the GF IP. The GF IP locations are indicated with dashed grey lines.

For the 1-ms-averaged data, the beam jitters interpolated to the GF IP were $\sigma_x = 65\,\mu\text{m}$ and $\sigma_y = 40\,\mu\text{m}$, calculated over 7000 samples of the flat-top. The beam stability across the flat-top, for five consecutive cycles, is shown in Fig. 3. The drifts observed throughout the flat-tops were 40-50 µm horizontally and 10-20 µm vertically. The cycle-to-cycle r.m.s variations were $\sigma_x = 50\,\mu\text{m}$ and $\sigma_y = 30\,\mu\text{m}$.

FFTs of the 1-ms-averaged data and the turn-by-turn data are presented in Fig. 4 and Fig. 5 respectively and the dominant frequency components are listed. The horizontal tune was 20.119, the vertical tune was 20.186 and the synchrotron tune was 0.0072 which corresponded to frequencies of 5.16 kHz, 8.05 kHz and 313.1 Hz, respectively.

The beam trajectory was fitted sample-by-sample to the dispersion function to estimate the momentum offset per sample. An FFT of these momentum offsets is given in Fig. 6. From this, the momentum stability was calculated as 2×10^{-5}, which agrees with previous measurements [5] which determined it to be better than 10^{-4}.

The r.m.s of the measured beam positions contains contributions from both the true beam position variation and also the BPM precision. To estimate the contribution from the BPM precision, Singular Value Decomposition (SVD) analysis was applied to the turn-by-turn data [2]. The data for m BPMs and n pulses were collated into $n \times m$ matrix B, and SVD analysis applied using the decomposition $B = U\Lambda V^T$, where Λ is a positive-definite diagonal matrix of singular values in decreasing order, U comprises the spatial vectors and V the temporal vectors.

The singular values from the SVD analysis are shown in Fig. 7. This method allowed for the separation of modes displaying high correlation between the BPMs and, thus, true beam jitter. Two of the dominant modes are shown in Fig. 8. Once the ten most correlated modes were subtracted from the data, the r.m.s was re-calculated from the remaining modes yielding an upper estimate for the turn-by-turn BPM precision of $\sim 200\,\mu\text{m}$. This suggests that the vertical beam jitter measurements were limited by the BPM precision. The corresponding

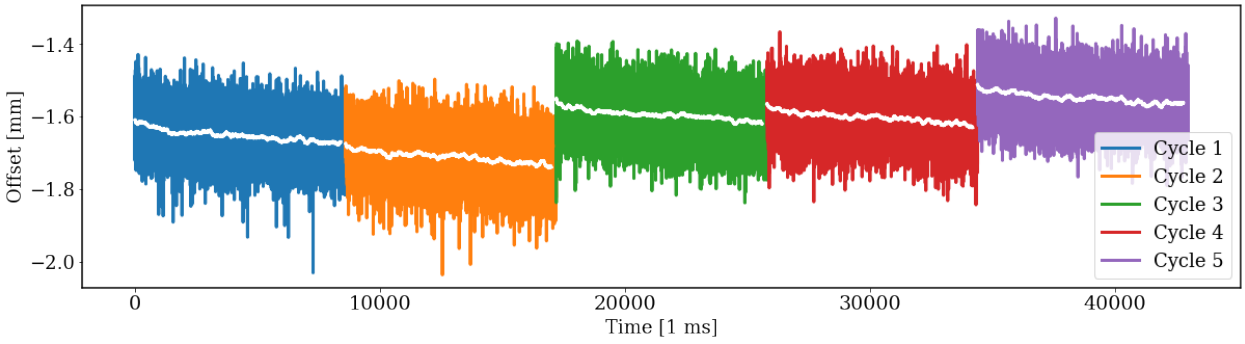

(a)

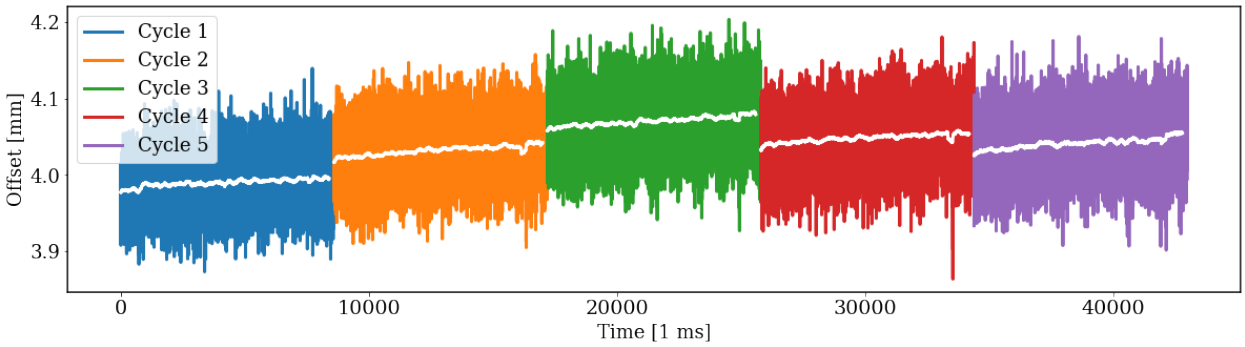

(b)

Figure 3: Beam position offset at the GF IP calculated using the beamline model and the 1-ms-averaged Orbit-mode data taken at surrounding BPMs, with (a) horizontal and (b) vertical beam positions across the flat-top (blue) with a 100-sample rolling average (orange); five consecutive cycles are shown.

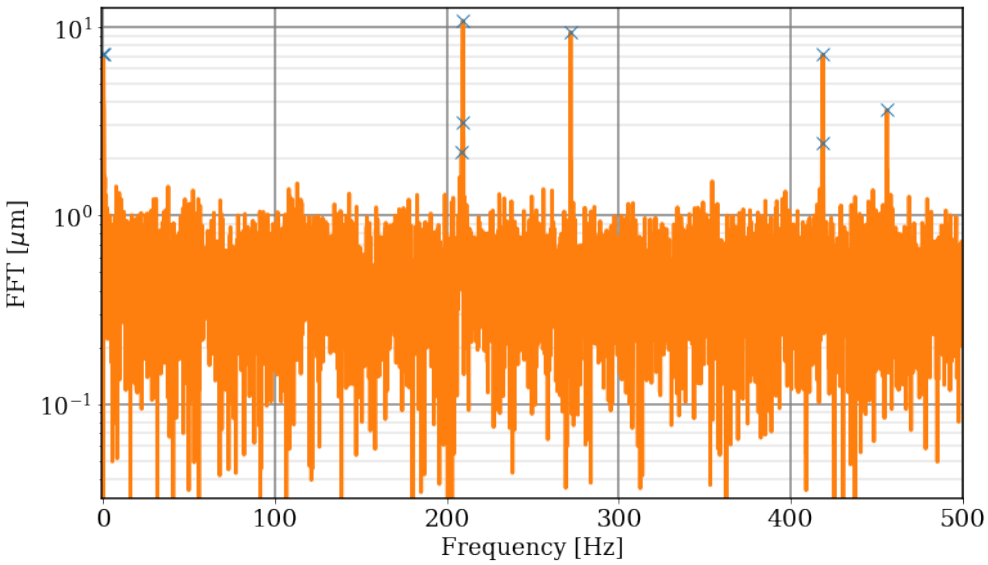

(a)

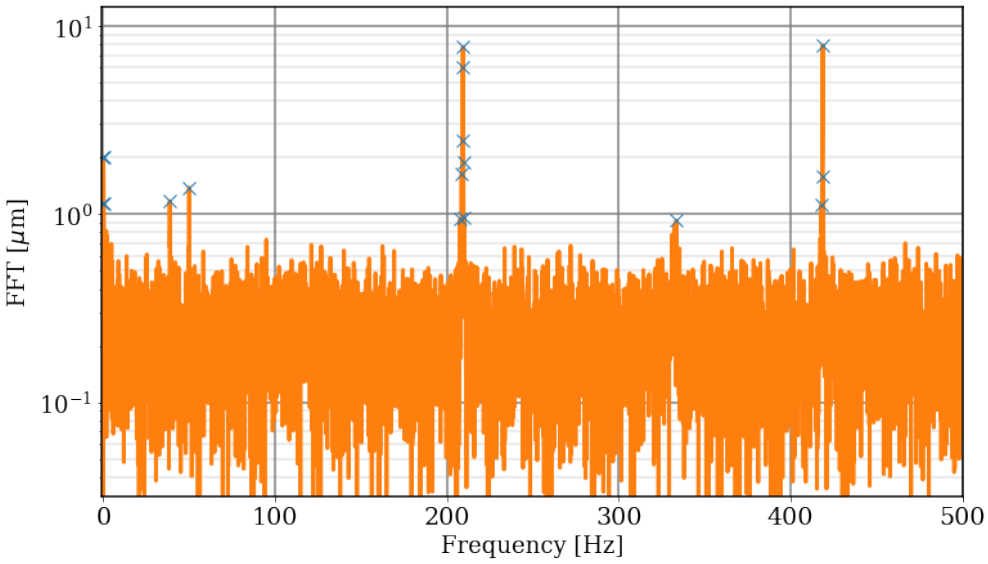

(b)

Figure 4: Normalised FFT of the (a) horizontal and (b) vertical 1 kHz beam positions averaged over all SPS BPMs for the flat-top of one cycle. The dominant frequencies seen in the horizontal data are 0.016 Hz, 208.8 Hz, 271.9 Hz, 418.4 Hz, 456.0 Hz, and in the vertical data they are 0.016 Hz, 38.7 Hz, 50.0 Hz, 208.6 Hz, 333.5 Hz 418.7 Hz. The data included 8600 samples giving a resolution of 0.12 Hz.

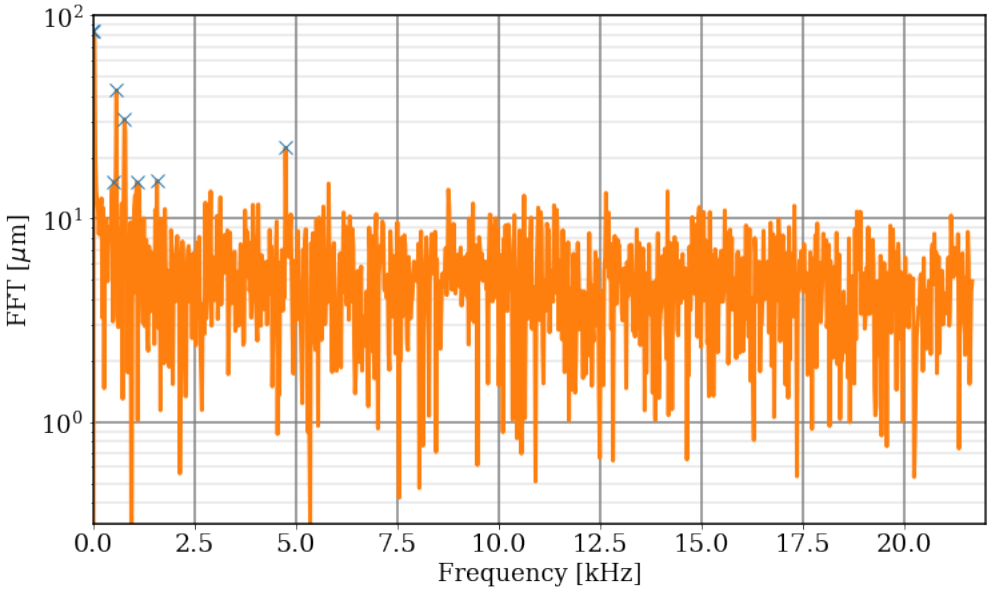

(a)

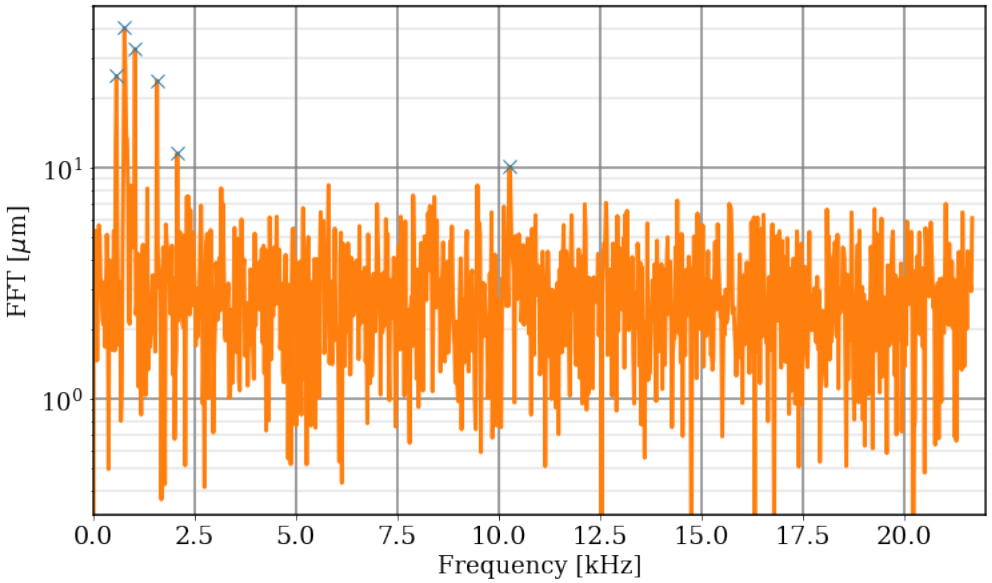

(b)

Figure 5: Normalised FFT of the (a) horizontal and (b) vertical turn-by-turn beam positions averaged for all SPS BPMs. The dominant frequencies seen in the horizontal data are 0.021, 0.520, 0.586, 1.084, 1.583, 4.749 kHz, and in the vertical data they are 0.586, 0.781, 1.041,1.583, 2.082, 10.257 kHz. The data included 2000 turns giving a resolution of 21.69 Hz.

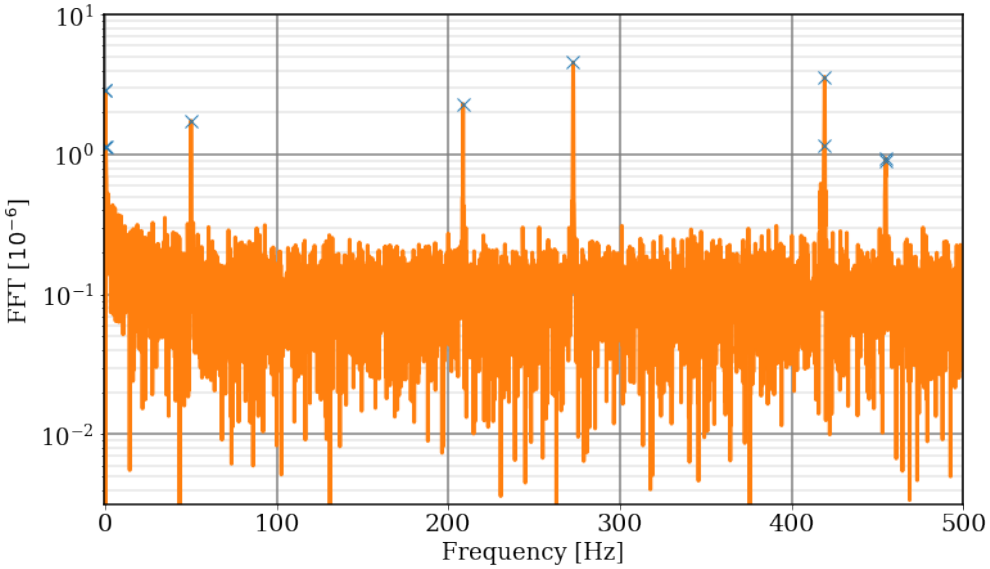

Figure 6: Normalised FFT of the sample-by-sample momentum offset estimated by fitting the 1 kHz BPM data to the dispersion function, the dominant frequency components are 0.016 Hz, 50 Hz, 207.4 Hz, 271.9 Hz, 418.7 Hz, 456.0 Hz. The data included 8600 samples giving a resolution of 0.12 Hz.

plots for the 1-ms-averaged data are shown in Fig. 9, producing a precision estimate of 30 µm. The peak in the second mode shown in Fig. 9 indicates a faulty BPM signal.

3 Control of the beam position at the GF IP

Four-corrector orbit bumps were used to vary the horizontal and vertical position of the beam at the GF IP. Correctors were selected so as to have the maximum effect at the IP with the smallest corrector strengths; these were ['60807', '61207', '62807', '63207'] horizontally and ['60907', '61107', '62907', '63107'] vertically. This combination of correctors allowed for the variation of the horizontal and vertical IP beam position up to ±1.5 mm and ±1.2 mm, respectively. A four-corrector orbit bump allowed for the position (Δx) and angle ($\Delta x'$) of the beam to be adjusted independently at location s, using deflection angles θ_i for the four

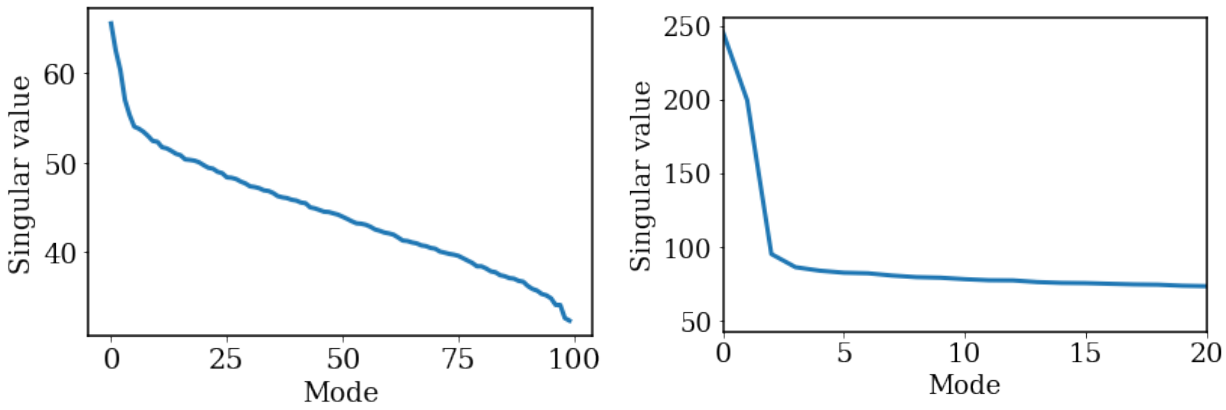

Figure 7: Singular values from the SVD analysis of (a) turn-by-turn and (b) 1-ms-averaged BPM vertical position data.

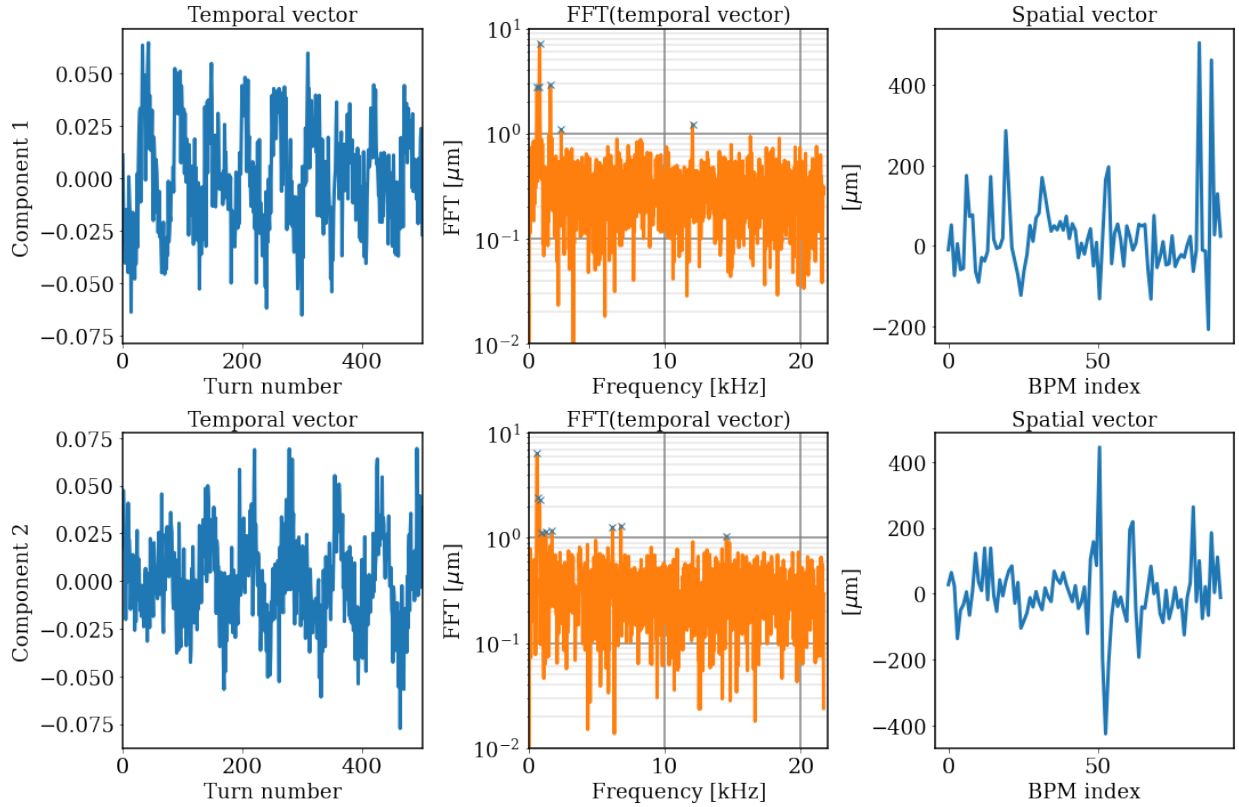

Figure 8: Temporal and spatial vectors from the SVD analysis of turn-by-turn BPM vertical position data. The FFT of the temporal vector is also shown, highlighting the main frequency components.

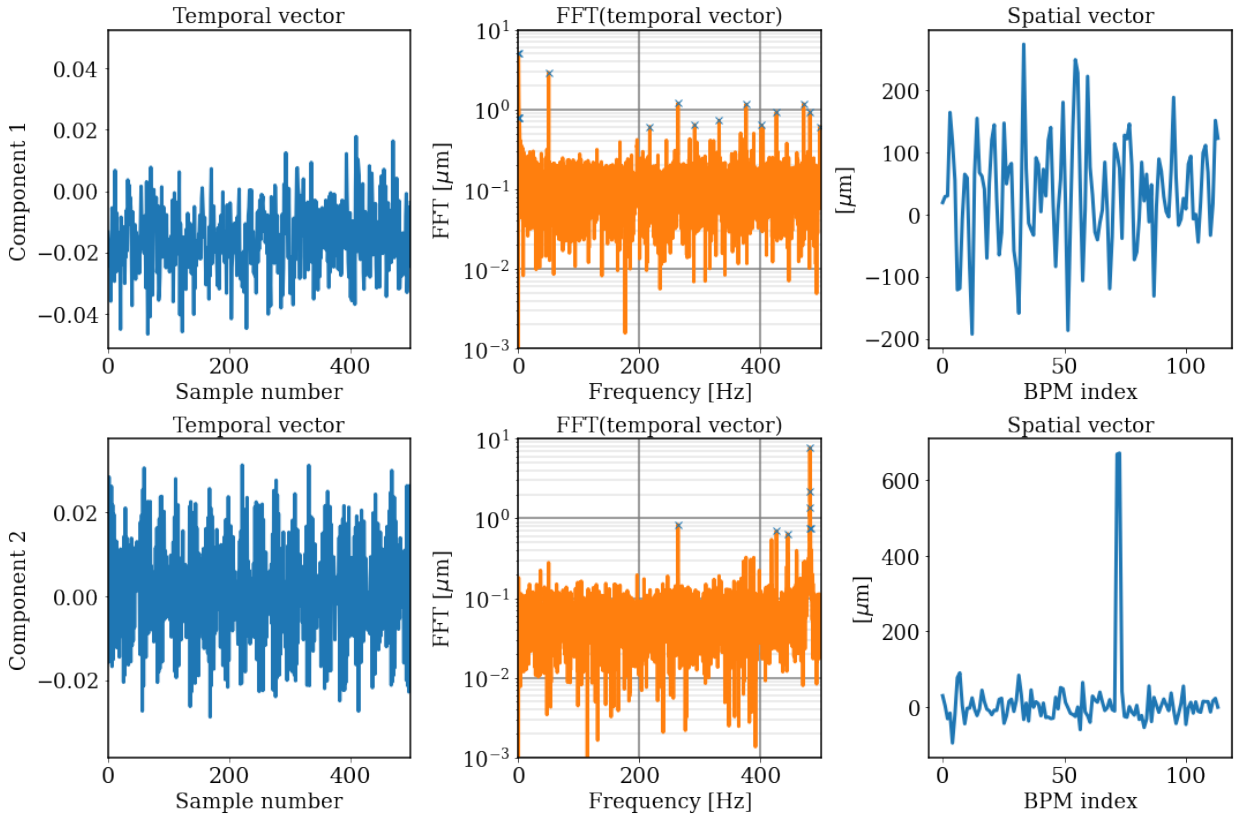

Figure 9: Temporal and spatial vectors from the SVD analysis of 1-ms-averaged BPM vertical position data. The FFT of the temporal vector is also shown, highlighting the main frequency components.

correctors where $i = 1, .., 4$ [4]:

$$\begin{aligned}
\theta_1 &= \frac{1}{\sqrt{\beta_1\beta_s}}\frac{\cos(\mu_s-\mu_2)-\alpha_s\sin(\mu_s-\mu_2)}{\sin(\mu_2-\mu_1)}\Delta x - \sqrt{\frac{\beta_s}{\beta_1}}\frac{\sin(\mu_s-\mu_2)}{\sin(\mu_2-\mu_1)}\Delta x', \\
\theta_2 &= -\frac{1}{\sqrt{\beta_2\beta_s}}\frac{\cos(\mu_s-\mu_1)-\alpha_s\sin(\mu_s-\mu_1)}{\sin(\mu_2-\mu_1)}\Delta x + \sqrt{\frac{\beta_s}{\beta_2}}\frac{\sin(\mu_s-\mu_1)}{\sin(\mu_2-\mu_1)}\Delta x', \\
\theta_3 &= -\frac{1}{\sqrt{\beta_3\beta_s}}\frac{\cos(\mu_s-\mu_4)-\alpha_s\sin(\mu_s-\mu_4)}{\sin(\mu_4-\mu_3)}\Delta x - \sqrt{\frac{\beta_s}{\beta_3}}\frac{\sin(\mu_s-\mu_4)}{\sin(\mu_4-\mu_3)}\Delta x', \\
\theta_4 &= \frac{1}{\sqrt{\beta_4\beta_s}}\frac{\cos(\mu_s-\mu_3)-\alpha_s\sin(\mu_s-\mu_3)}{\sin(\mu_4-\mu_3)}\Delta x + \sqrt{\frac{\beta_s}{\beta_4}}\frac{\sin(\mu_s-\mu_3)}{\sin(\mu_4-\mu_3)}\Delta x'.
\end{aligned} \tag{1}$$

The simulation of the beam trajectory for a 1 mm orbit bump is shown in Fig. 10; the orbit bump amplitude is here defined at the GF IP.

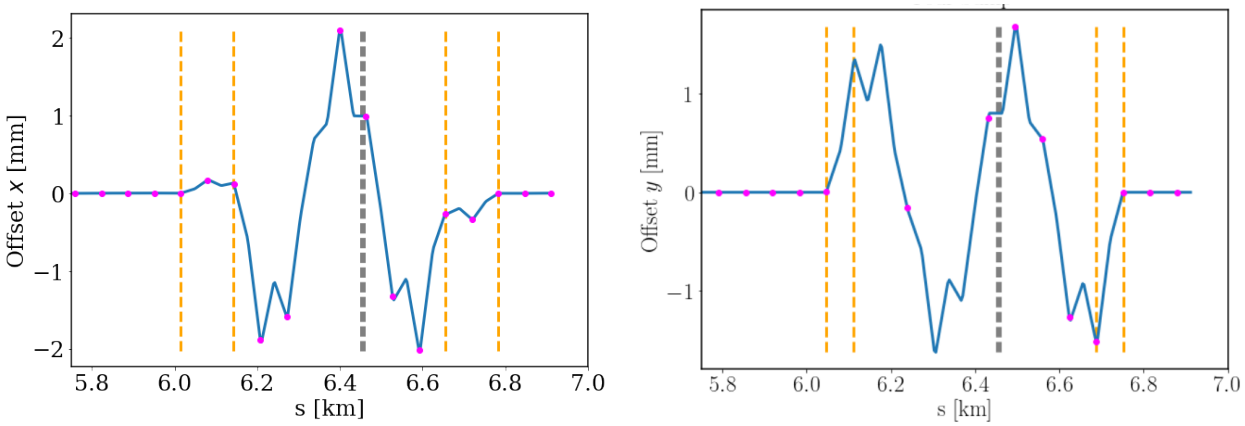

(a) (b)

Figure 10: MAD-X simulation of (a) horizontal and (b) vertical four-corrector orbit bumps producing a 1 mm position offset with zero angle offset at the GF IP. The location of the GF IP is indicated with a gray dotted line, the locations of the orbit bump correctors are in orange and the locations of the BPMs for the relevant plane are shown in magenta.

The beam position variation throughout the position scan is presented in Fig. 11 for BPMs in the region of the GF IP. These data show that, during the position scan, the orbit variation outside of bump is similar to stable operation suggesting the orbit bump is well closed.

The beam was scanned ±1 mm horizontally and vertically to study the beam control and the stability throughout the scan. The beam position at the GF IP was determined by interpolating measurements from surrounding BPMs, with all positions considered relative to the average nominal trajectory. Figure 12 shows the BPM data across the orbit bump scan, with the interpolated beam trajectories overlaid. The interpolated beam positions at the GF IP were compared with the intended orbit bump amplitude, this is presented in Fig. 13. The vertical results in particular show good agreement between the model predictions and the measured data.

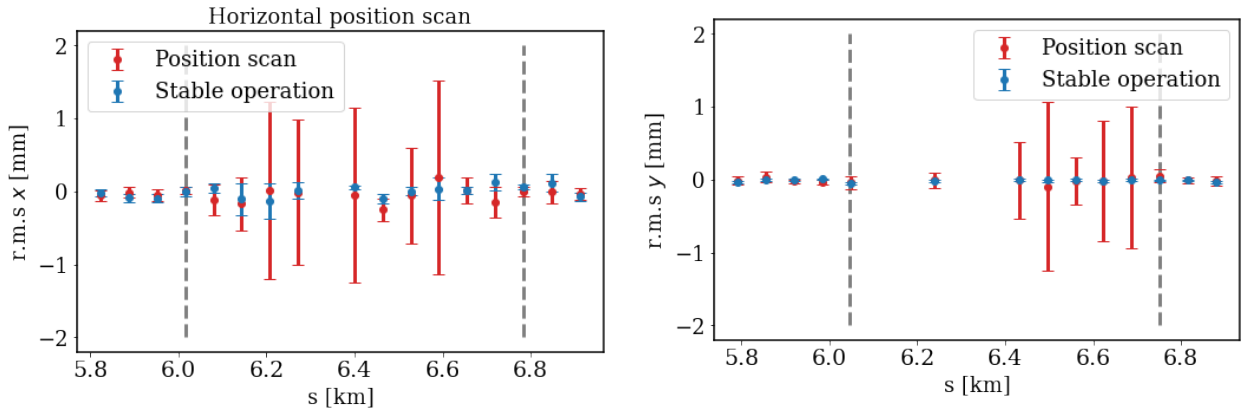

(a) (b)

Figure 11: Beam position r.m.s variation throughout (a) horizontal and (b) vertical position scans with four-corrector orbit bumps, showing their correct closure. The grey dotted lines show the outer limits of the orbit bumps.

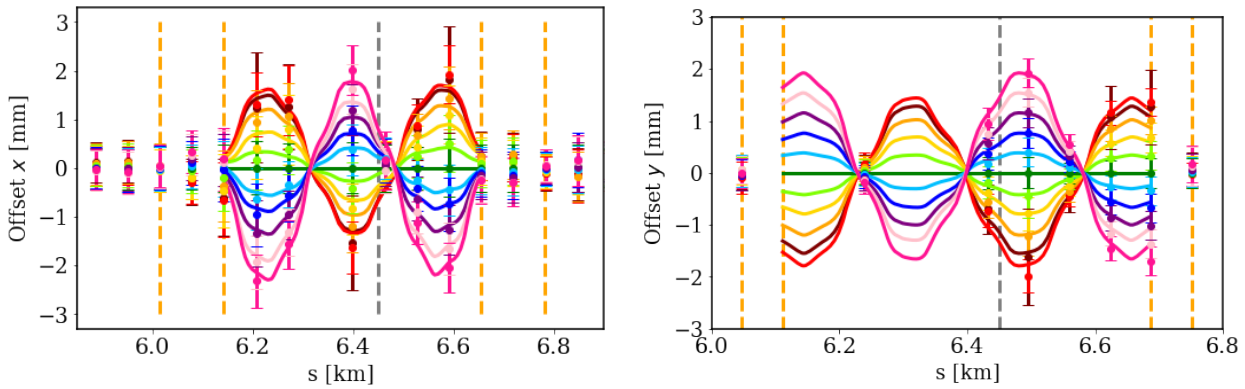

(a) (b)

Figure 12: Beam position measurements for (a) horizontal and (b) vertical four-corrector orbit bumps. The mean and standard deviation of the data are given by the data points and errorbars, respectively; the estimated beam trajectories are given by the solid lines; the orange dotted lines highlight the corrector locations and the grey dotted line the GF IP. Each orbit bump setting is shown with a single colour.

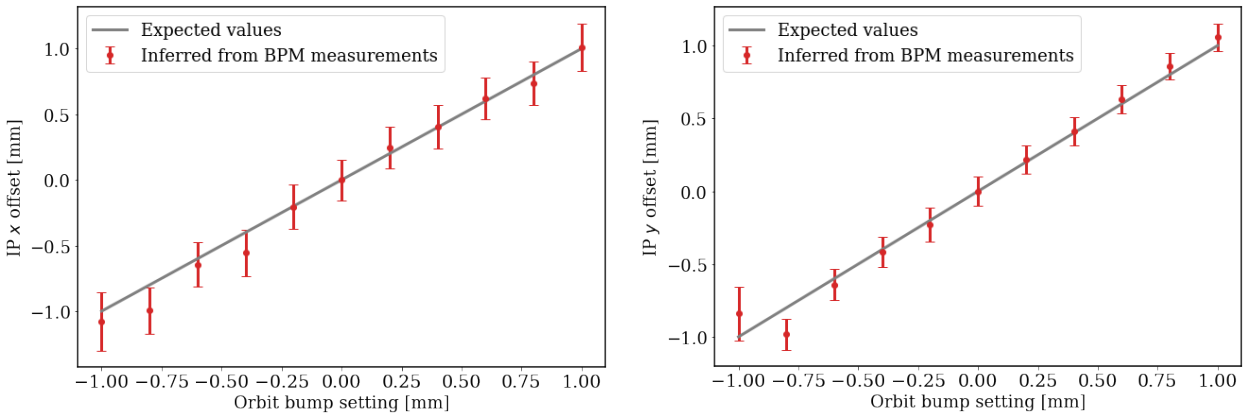

(a) (b)

Figure 13: Beam position measurements propagated to the GF IP for (a) horizontal and (b) vertical four-corrector orbit bumps. Measured results are shown in red compared with the predicted trend shown in grey.

For a 1 mm horizontal orbit bump, simulations show that the beam path length would be expected to increase by 0.228 mm, which would increase the average radial position by approximately 36.3 µm. This is consistent with measured data which show a 37 µm increase in average radial position for a 1 mm orbit bump at the GF IP (Fig. 14). Excluding the outlier in Fig. 14 (at 0.2 mm bump height), the measurement-simulation-difference for the orbit bump height (Fig. 13(a)) and the average radial position (Fig. 14) have a 75% correlation.

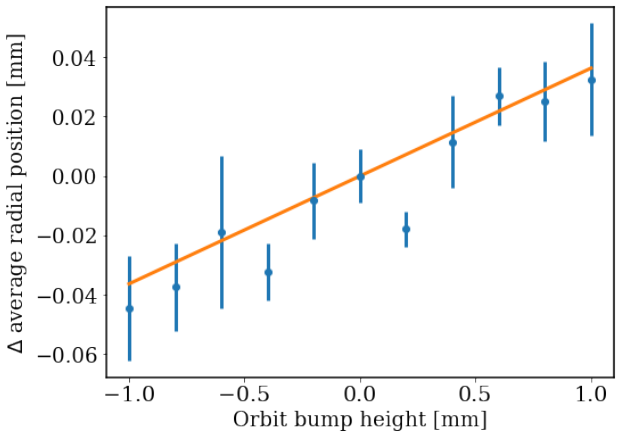

Figure 14: The change in average orbit radius as a function of the orbit bump height at the GF IP for the horizontal orbit bump scan (see Fig. 13(a)); the data points show the median value at each orbit bump setting and the errorbar the standard deviation, the expected trend from simulations is shown in orange.

4 Control over the beam momentum with radial steering

The SPS radial steering was used to vary the flat-top fixed frequency and, consequently, the revolution frequency and orbit radius. The nominal flat-top frequency was $f_0 = 43.372\,\mathrm{kHz}$. The orbit radius ($R$) varied with the revolution frequency (f) as [1],

$$\frac{\mathrm{d}\cancelto{0}{B}}{\cancel{B}} = \gamma^2 \frac{\mathrm{d}f}{f} + (\gamma^2 - \gamma_t^2)\frac{\mathrm{d}R}{R}, \tag{2}$$

where B was the magnetic field, the Lorentz $\gamma = 251.635$, and the transition γ, $\gamma_t = 17.95$. From this relation, a change in revolution frequency of $-0.039\,36\,\mathrm{Hz}$ corresponds to a $1\,\mathrm{mm}$ change in orbit radius. The radius of the beam orbit could safely be varied in this way up to $1\,\mathrm{cm}$ which corresponded to a position shift at the GF IP of approximately a quarter of this value. The change in momentum, $\frac{\mathrm{d}p}{p}$, relates to the change in orbit radius as [1],

$$\frac{\mathrm{d}p}{p} = \gamma_t^2 \frac{\mathrm{d}R}{R}. \tag{3}$$

The change in beam trajectory across the radial steering scan is shown in Fig. 15(a). The beam trajectories shown were calculated by fitting the form (X_n-values) of the beam trajectory ($X_1 \sin(2\pi\mu(s)+X_2)+X_3 D(s)$) to the BPM data, where $\mu(s)$ is the phase advance and $D(s)$ is the dispersion, for longitudinal position s. X_3 then represents the change in momentum ($\mathrm{d}p/p$) so that the measurements could be compared with the relation shown in Eq. 3. This comparison is presented in Fig. 15(b), showing good agreement between the expected and measured values.

5 Conclusions

The SPS beam stability was investigated for the region of the proposed GF IP. The measured beam jitter, both turn-by-turn and cycle-to-cycle (Table 1), are within the range to be suitable for the GF experiment. The beam jitter measurements appeared to be limited by the BPM precision suggesting the true beam jitter is even lower. The beam position at the IP could be controlled well with a four-corrector orbit bump, independently of the beam angle. The measured beam trajectory followed closely the predictions from simulations. Radial steering was implemented to vary the revolution frequency and in turn the momentum and orbit radius. Throughout the scan of radial steering, the change in momentum and change in orbit radius showed excellent agreement with their expected linear relationship.

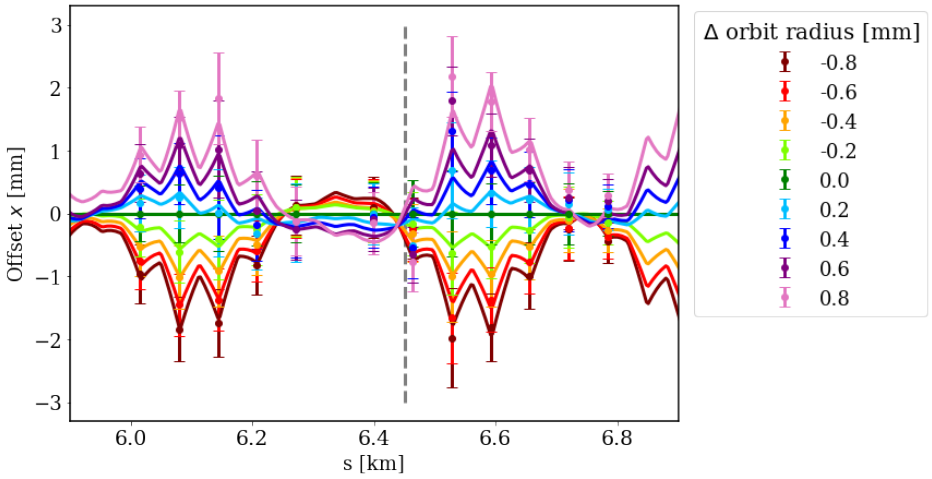

(a)

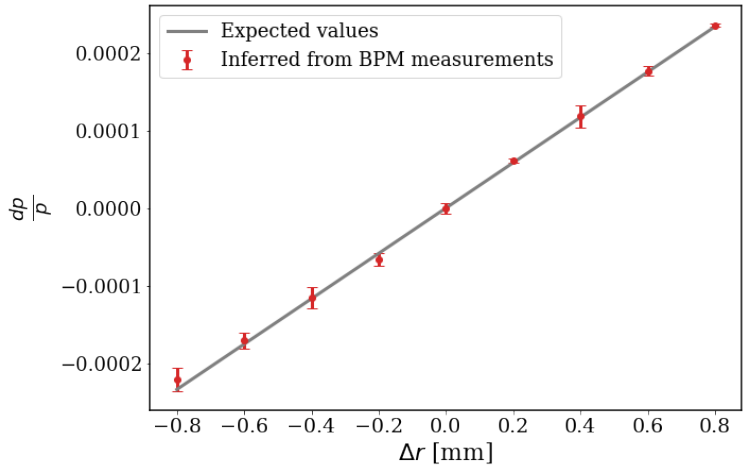

(b)

Figure 15: Measurements from a scan of the revolution frequency. (a) The data points show the mean and standard deviation of the beam positions at the BPMs relative to the nominal setting. The line shows the beam trajectory fitted to the data. (b) The change in momentum and change in orbit radius at the GF IP, determined from the change in beam trajectories, is compared with the expected trend (see Eq. 3).

Parameter	Stability (r.m.s)	Frequencies observed
Momentum offset	2×10^{-5}	0.016, 50, 207.4, 271.9, 418.7, 456.0 Hz
Orbit (x, 1-ms-averaged)	65 µm	0.016, 208.8, 271.9, 418.4, 456.0 Hz
Orbit (y, 1-ms-averaged)	40 µm	0.016, 38.7, 50.0, 208.6, 418.7 Hz
Orbit (x, turn-by-turn)	450 µm	0.021, 0.520, 0.586, 1.084, 1.583, 4.749 kHz
Orbit (y, turn-by-turn)	250 µm	0.586, 0.781, 1.041,1.583, 2.082, 10.257 kHz
Orbit (x, cycle-to-cycle)	50 µm	
Orbit (y, cycle-to-cycle)	30 µm	

Table 1: Stability of measured parameters at the GF IP and the dominant frequencies observed in their respective FFTs.

References

[1] A. W. Chao et al. *Handbook of accelerator physics and engineering*. World scientific, 2013.

[2] J. Irwin, C. X. Wang, Y. T. Yan, K. Bane, Y. Cai, F. Decker, M. Minty, G. Stupakov, and F. Zimmermann. Model-independent analysis with BPM correlation matrices. Technical report, Stanford Univ., Stanford Linear Accelerator Center, CA (US), 1998.

[3] M. W. Krasny et al. Gamma Factory Proof-of-Principle Experiment. Technical Report CERN-SPSC-2019-031, SPSC-I-253, CERN, Geneva, Switzerland, September 2019.

[4] R. J. Steinhagen. LHC Beam Stability and Feedback Control. Technical Report CERN-AB-2007-049, CERN, Geneva, Switzerland, September 2007.

[5] J. Wenninger. SPS Momentum Calibration and Stability in 2003. Technical Report CERN-AB-Note-2003-091-OP, CERN, Geneva, Switzerland, 2003.